# REVERBERATION MAPPING OF THE *KEPLER*-FIELD AGN KA1858+4850

Liuyi Pei[1], Aaron J. Barth[1], Greg S. Aldering[2], Michael M. Briley[3], Carla J. Carroll[4], Daniel J. Carson[1], S. Bradley Cenko[5,6,7], Kelsey I. Clubb[8], Daniel P. Cohen[8], Antonino Cucchiara[2,8], Tyler D. Desjardins[9], Rick Edelson[5], Jerome J. Fang[10], Joseph M. Fedrow[11,12], Alexei V. Filippenko[8], Ori D. Fox[8], Amy Furniss[13], Elinor L. Gates[14], Michael Gregg[15], Scott Gustafson[16], J. Chuck Horst[11], Michael D. Joner[4], Patrick L. Kelly[8], Mark Lacy[17], C. David Laney[4], Douglas C. Leonard[11], Weidong Li[8,18], Matthew A. Malkan[19], Bruce Margon[10], Marcel Neeleman[16], My L. Nguyen[20], J. Xavier Prochaska[10,21], Nathaniel R. Ross[18], David J. Sand[22,23], Kinchen J. Searcy[24], Isaac S. Shivvers[8], Jeffrey M. Silverman[25], Graeme H. Smith[21], Nao Suzuki[26], Krista Lynne Smith[5], David Tytler[16], Jessica K. Werk[10,21], and Gábor Worseck[21]

*Draft version September 2, 2014*

## ABSTRACT

KA1858+4850 is a narrow-line Seyfert 1 galaxy at redshift 0.078 and is among the brightest active galaxies monitored by the *Kepler* mission. We have carried out a reverberation mapping campaign designed to measure the broad-line region size and estimate the mass of the black hole in this galaxy. We obtained 74 epochs of spectroscopic data using the Kast Spectrograph at the Lick 3-m telescope from February to November of 2012, and obtained complementary *V*-band images from five other ground-based telescopes. We measured the H$\beta$ light curve lag with respect to the *V*-band continuum light curve using both cross-correlation techniques (CCF) and continuum light curve variability modeling with the JAVELIN method, and found rest-frame lags of $\tau_{\mathrm{CCF}} = 13.53^{+2.03}_{-2.32}$ days and $\tau_{\mathrm{JAVELIN}} = 13.15^{+1.08}_{-1.00}$ days. The H$\beta$ root-mean-square line profile has a width of $\sigma_{\mathrm{line}} = 770 \pm 49$ km s$^{-1}$. Combining these two results and assuming a virial scale factor of $f = 5.13$, we obtained a virial estimate of $M_{\mathrm{BH}} = 8.06^{+1.59}_{-1.72} \times 10^6 \, M_\odot$ for the mass of the central black hole and an Eddington ratio of $L/L_{\mathrm{Edd}} \approx 0.2$. We also obtained consistent but slightly shorter emission-line lags with respect to the *Kepler* light curve. Thanks to the *Kepler* mission, the light curve of KA1858+4850 has among the highest cadences and signal-to-noise ratios ever measured for an active galactic nucleus; thus, our black hole mass measurement will serve as a reference point for relations between black hole mass and continuum variability characteristics in active galactic nuclei.

[1] Department of Physics and Astronomy, University of California, Irvine, CA, 92697, USA
[2] Lawrence Berkeley National Laboratory, Berkeley, CA 94720, USA
[3] Department of Physics and Astronomy, Appalachian State University, Boone, NC 28608, USA
[4] Department of Physics and Astronomy, N283 ESC, Brigham Young University, Provo, UT 84602, USA
[5] Department of Astronomy, University of Maryland, College Park, MD 20742, USA
[6] Astrophysics Science Division, NASA Goddard Space Flight Center, Mail Code 661, Greenbelt, MD 20771, USA
[7] Joint Space Science Institute, University of Maryland, College Park, MD 20742, USA
[8] Department of Astronomy, University of California, Berkeley, CA 94720-3411, USA
[9] Department of Physics and Astronomy, The University of Western Ontario, London, ON, N6A 3K7, Canada
[10] Department of Astronomy and Astrophysics, University of California, Santa Cruz, 1156 High Street, Santa Cruz, CA 95064, USA
[11] Department of Astronomy, San Diego State University, San Diego, CA 92182, USA
[12] Center for Astrophysics and Space Sciences, University of California, San Diego, La Jolla, CA 92093, USA
[13] Department of Physics, Stanford University, 382 Via Pueblo Mall, Stanford, CA 94305, USA
[14] Lick Observatory, P.O. Box 85, Mt. Hamilton, CA 95140
[15] Department of Physics, University of California, Davis, One Shields Ave, Davis, CA 95616, USA
[16] Department of Physics, University of California, San Diego, La Jolla, CA 92093, USA
[17] NRAO, 520 Edgemont Road, Charlottesville, VA 22903, USA
[18] Deceased 12 December 2011
[19] Department of Physics and Astronomy, University of California, Los Angeles, CA 90095, USA
[20] Department of Physics and Astronomy, University of Wyoming, 1000 E. University Ave. Laramie, WY 82071, USA
[21] Department of Astronomy and Astrophysics, UCO/Lick Observatory, University of California, 1156 High Street, Santa Cruz, CA 95064, USA
[22] Las Cumbres Observatory Global Telescope Network, 6740 Cortona Drive, Suite 102, Goleta, CA 93117, USA
[23] Department of Physics, Texas Tech University, Lubbock, TX 79409, USA
[24] San Diego Astronomy Association, P.O Box 23215, San Diego, CA 92193, USA
[25] Department of Astronomy, University of Texas at Austin, 2515 Speedway, Stop C1400, Austin, Texas 78712, USA
[26] Kavli Institute for Particle Astrophysics and Cosmology, Stanford University, 452 Lomita Mall, Stanford, CA 94305, USA

## 1. INTRODUCTION

The NASA *Kepler* Mission, designed to search for exoplanets, continuously monitored the brightness of more than $100,000$ stars in a 115 square-degree field for about four years (Borucki et al. 2010). Situated within the *Kepler* field are several active galactic nuclei (AGNs) that also exhibit optical flux variations. *Kepler*'s monitoring capabilities enable measurements of AGN optical light curves over long temporal baselines with unprecedented cadence and precision, providing the basis for extremely detailed AGN variability studies.

Observations have revealed correlations between AGN variability amplitude and redshift (Cristiani et al. 1990; Giallongo et al. 1991; Hook et al. 1994; Cid Fernandes et al. 1996; Vanden Berk et al. 2004), variability amplitude and black hole mass (Wold et al. 2007; Wilhite et al. 2008; Bauer et al. 2009), and anticorrelations between variability amplitude and luminosity (Cristiani et al. 1990; Hook et al. 1994; Cid Fernandes et al. 1996; Giveon et al. 1999; Vanden Berk et al. 2004; Webb & Malkan 2000). Furthermore, analyses of continuum light curves have revealed the presence of characteristic variability timescales which have been found to vary with black hole mass (Collier & Peterson 2001; MacLeod et al. 2010). The *Kepler* high-resolution light curves have a cadence of 30 minutes, and are the only datasets to date that have been able to probe optical AGN variability down to such short time scales. Optical fluctuation power spectral density functions for several *Kepler* AGNs have already been published (Mushotzky et al. 2011), and they have shown much steeper slopes than those seen in the X-rays. *Kepler*'s light curves provide new high signal-to-noise ratio (SNR) data which will test and better constrain these previously established correlations and further shed light on AGN variability characteristics.

Independent measurements of black hole mass are required to search for connections between AGN variability characteristics and black hole mass. To this end, we present the results of a nine-month monitoring campaign for the narrow-line Seyfert 1 (NLS1) galaxy 1RXSJ185800.9+485020, also known as KA1858+4850, which has redshift $z = 0.078$ and a Galactic extinction of $A_V = 0.15$ mag (Schlafly & Finkbeiner 2011). This object was identified as an X-ray source in the *ROSAT* All-Sky Bright Source Catalogue (Voges et al. 1999). Prior to 2012, there was no published spectrum of KA1858+4850 in the literature, and an observation from Lick Observatory identified it as a Seyfert 1 galaxy (Edelson & Malkan 2012). The initial portion of KA1858+4850's *Kepler* light curve from quarters Q6 and Q7 was published by Mushotzky et al. (2011) and showed strong optical variability, qualifying it as a prime candidate for reverberation mapping.

The technique of reverberation mapping relies on the assumption that variability in the AGN continuum is echoed by emission lines originating from the surrounding broad-line region (BLR; Blandford & McKee 1982). Ionizing photons from the AGN central engine travel to the BLR gas in a time $\tau$ that is a function of the BLR radius. Changes in the ionizing photon flux incident on BLR clouds cause fluctuations in the emission-line flux.

This means that the emission-line light curve will appear as a lagged version of the continuum light curve, and the lag time, combined with the speed of light, can give an estimate of the BLR radius. Additionally, the line-emitting gas orbits the central black hole at very high velocities, which causes Doppler broadening of the emitted spectral lines. The width of the broad emission line gives the velocity dispersion of the BLR gas, which, combined with the BLR radius, can yield a virial estimate of the central black hole mass.

*Kepler* light curves covering over two years of monitoring are now publicly available for KA1858+4850, of which three consecutive quarters (Q13, Q14, and Q15) directly coincide with the time of our ground-based monitoring campaign. We therefore performed our analysis using both $V$-band and *Kepler* observations.

We employed the Lick Observatory 3-m Shane telescope with the Kast Spectrograph and five other ground-based telescopes to spectroscopically and photometrically monitor KA1858+4850 from February to November of 2012. We describe our imaging observations and data reductions in §2 and §3; spectroscopic observations, reductions, and measurements are described in §4 and §5; §6 outlines the steps in measuring emission-line light curve lags; our estimates of the black hole mass ($M_{\rm BH}$) and Eddington ratio are discussed in §7 and §8; and §9 summarizes our results.

## 2. IMAGING OBSERVATIONS

Reverberation mapping requires a continuum light curve with high sampling cadence and SNR. To achieve this, we obtained $V$-band images from ground-based telescopes and used aperture photometry to construct a light curve for KA1858+4850 that has nearly nightly sampling for a span of 290 days. For several reasons, we chose to use the $V$-band light curve rather than the *Kepler* light curve for reverberation measurements. First, we wanted to monitor the AGN's variability in real time, and since *Kepler* data are uploaded only periodically, this was possible only with ground-based monitoring. Additionally, the *Kepler* passband, at $4000-8650$ Å, includes the strong H$\alpha$ emission line, which can contribute significantly to the photometric fluxes and introduce a strong lag signal to what should ideally be a pure continuum light curve. Furthermore, *Kepler* light curves exhibit severe mismatches between the flux scales for different quarterly observation sets, as can be seen in light curves shown by Revalski et al. (2014). We avoided these issues by constructing the continuum light curve with photometric data from five ground-based telescopes, whose properties are described in the following sections.

### 2.1. *West Mountain Observatory*

The Brigham Young University West Mountain Observatory (WMO) uses a 0.9-m telescope that employs a FLI PL3041UV detector with a $20.'8 \times 20.'8$ field of view. The CCD has 15 $\mu$m pixels and a scale of $0.''61$ pixel$^{-1}$. KA1858+4850 was observed at WMO with exposure times of 200 s, 240 s, 250 s, or 300 s. WMO data covered the period from March to November of 2012 with images from 124 nights, and had a median seeing of $3.''2$. Figure 1 shows a portion of the WMO field of view centered on KA1858+4850.

## 2.2. *KAIT*

The Katzman Automatic Imaging Telescope (KAIT) at Lick Observatory is a 0.76-m robotic telescope with an Apogee AP7 CCD, which has 24 $\mu$m pixels in a $500 \times 500$ array and a scale of $0''.8$ pixel$^{-1}$ (Filippenko et al. 2001). KA1858+4850 was observed with KAIT using 300 s exposures with the exception of six nights, for which exposure times of 60 s, 180 s, or 240 s were used. The median seeing for the KAIT exposures was $3''.2$, and the observing period at KAIT spanned February to September of 2012 with data from 109 nights.

## 2.3. *Faulkes Telescope North*

The Faulkes Telescope North (FTN), operated by the Las Cumbres Observatory Global Telescope Network, is a 2-m telescope located at the Haleakala Observatory in Hawaii. We used the Spectral camera with a Fairchild Imaging CCD486 detector, which has a $10'.5 \times 10'.5$ field of view (Brown et al. 2013). The CCD has 15 $\mu$m pixels in a $4000 \times 4000$ array and has a scale of $0''.152$ pixel$^{-1}$. The images were obtained using $2 \times 2$ binning for the readout. KA1858+4850 was observed at FTN with 120 s exposures from February to March 2012. The exposure time was increased to 180 s in April 2012, then to 240 s in May for the remainder of the program ending in November. We obtained 65 epochs of data from FTN, with median seeing of $1''.6$.

## 2.4. *The Nickel Telescope*

The 1-m Nickel telescope at Lick Observatory employs a Loral $2048 \times 2048$ CCD with a $6'.3 \times 6'.3$ field of view and a scale of $0''.184$ pixel$^{-1}$. The images were obtained using $2 \times 2$ binning for the readout. KA1858+4850 was observed on the Nickel adopting 300 s exposures with the exception of three nights, for which 150 s, 250 s, and 600 s exposures were used. We obtained 47 epochs of data from the Nickel between February and November of 2012, and the median seeing was $2''.4$.

## 2.5. *Mount Laguna Observatory*

The Mount Laguna Observatory (MLO) 1-m telescope uses a Fairchild CCD that has 15 $\mu$m pixels in a $2048 \times 2048$ array, and has a scale of $0''.41$ pixel$^{-1}$. KA1858+4850 was observed at MLO with 300 s exposures. The median seeing for the MLO exposures was $3''.0$. Between February and November of 2012, we obtained 27 epochs of data from MLO.

## 3. PHOTOMETRIC REDUCTIONS AND MEASUREMENTS

### 3.1. *V-Band Data*

Photometric data reduction included overscan correction, trimming, bias subtraction, and flat fielding for all images. We used the *Astrometry.net* software (Lang et al. 2010) to register celestial coordinates onto images from WMO, KAIT, Nickel, and MLO. This step was omitted for FTN data, which already contained celestial coordinates in the image headers. After cleaning all images of cosmic rays using the L.A.Cosmic algorithm (van Dokkum 2001), we performed aperture photometry in IDL using an aperture radius of $3''$ and sky annulus radii of $10''-20''$, and obtained instrumental magnitudes for KA1858+4850 and seven comparison stars (marked
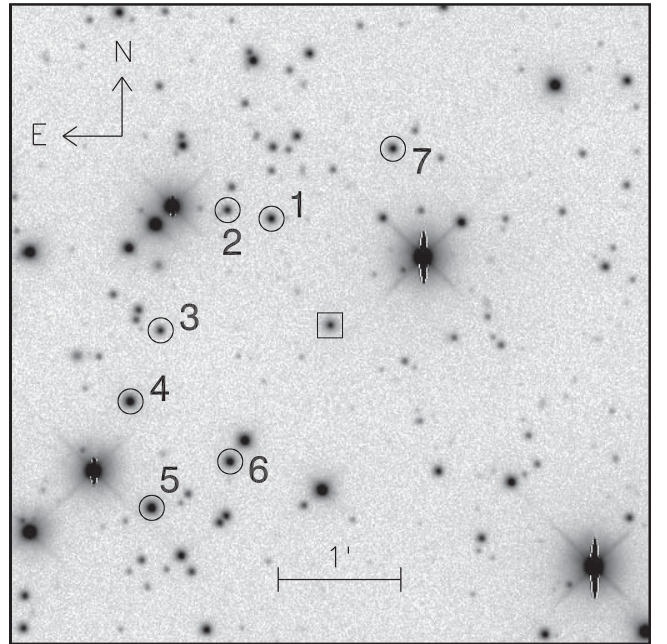


FIG. 1.— A subset of a coadded frame created from WMO images showing KA1858+4850 (boxed) and its seven comparison stars (circled).

in Figure 1) for each image. The comparison stars were chosen to have similar or slightly brighter $V$-band magnitudes compared to KA1858+4850. For nights where multiple exposures were taken at the same telescope, the magnitude measurements for each object were averaged into a single value. Since KA1858+4850 is almost indistinguishable from a point source at ground-based resolution, we did not attempt to remove host-galaxy light from the AGN photometry.

We used the comparison stars as constant-flux references and obtained a separate AGN light curve for each telescope. However, the uncertainties from aperture photometry photon counting errors underestimate the true photometric error budget. Additional sources of error include inconsistencies in flat-field corrections and poor comparison-star magnitude measurements owing to blemishes on the detector. We measured the magnitude of these additional errors by calculating the excess variance, defined as

$$\sigma_{\mathrm{x}}^2 = \frac{1}{N} \sum_{i=1}^{N} [(X_i - \mu)^2 - \sigma_i^2], \qquad (1)$$

in the scaled comparison-star light curves. Here, $N$ is the number of measurements in the sample, $\mu$ is the mean magnitude, and $X_i$ and $\sigma_i$ are the individual measurements and their associated uncertainties, respectively. The $\sigma_i$ values range from 0.004 mag to 0.048 mag, and the median and standard deviation of the uncertainties are 0.009 mag and 0.007 mag, respectively. We found the mean scatter of all seven comparison stars to be $\sigma_{\mathrm{x}} \approx 0.001$ mag, and added this in quadrature to the uncertainties from aperture photometry to produce the final AGN light curve for each telescope.

To combine the light curves from different telescopes, we scaled each light curve so that the mean comparison-star magnitudes for each telescope matched those from

| Star | $\alpha$ (h:m:s) | $\delta$ (○:′:″) | $V$ (mag) |
|---|---|---|---|
| 1 | 18:58:04.03 | 48:51:15.53 | $16.612 \pm 0.026$ |
| 2 | 18:58:06.24 | 48:51:19.82 | $17.121 \pm 0.037$ |
| 3 | 18:58:09.54 | 48:50:20.69 | $17.256 \pm 0.031$ |
| 4 | 18:58:11.03 | 48:49:46.16 | $15.449 \pm 0.028$ |
| 5 | 18:58:09.97 | 48:48:54.06 | $15.195 \pm 0.029$ |
| 6 | 18:58:06.09 | 48:49:16.65 | $15.843 \pm 0.029$ |
| 7 | 18:57:58.01 | 48:51:49.72 | $16.724 \pm 0.027$ |

Note. — Coordinates are J2000 and are based on an astrometric solution obtained by the *astrometry.net* software (Lang et al. 2010). The quoted uncertainties are calculated as the standard deviation of 18 measurements from photometric nights at WMO.

WMO, the telescope with the highest SNR and cadence and longest temporal coverage. However, each telescope has a different wavelength-dependent throughput, which can cause systematic offsets between light curves from different telescopes since the AGN is likely bluer than the average comparison-star color. We tested for these offsets by calculating the differences between AGN magnitude measurements taken on the same night but at different sites, and found the offsets to be on the order of 0.01 mag. We applied these calculated shifts to the FTN, KAIT, MLO, and Nickel light curves and brought them into agreement with WMO to produce the combined light curve.

Finally, we used Landolt (1992) standard stars observed at WMO to calibrate the zero point of the magnitude scale and produce the final light curve. We used WMO images from 18 nights, on which the observers deemed conditions photometric, to calibrate the comparison-star magnitudes. We did not attempt to compute color dependence in the Landolt calibrations.

Because truly photometric conditions are rare and difficult to confirm, each night gave slightly different comparison-star magnitudes. We took the weighted mean magnitude and standard deviation over 18 nights to be the magnitude and uncertainty for each star. The $V$ magnitudes of the comparison stars are listed in Table 1.

Figure 2 plots the final $V$-band light curve for KA1858+4850. The vertical length at each epoch indicates the photometric uncertainties, and the data are listed in Table 2. We averaged photometric measurements taken within 12 hours of each other to produce a condensed light curve that was used for subsequent lag analyses.

The steps from performing aperture photometry to obtaining a multiple-telescope light curve were carried out using an automated pipeline. Mapping WCS coordinates onto the images allowed for automatic detection of the AGN and comparison-star locations for aperture photometry. The automated nature of this process enables the pipeline to process a large number of images at once, and to rapidly produce and update the AGN light curve as new images are acquired.

### 3.2. *Kepler Data*

We also obtained *Kepler* Simple Aperture Photometry (SAP) fluxes for KA1858+4850 from the MAST archive for Q13, Q14, and Q15, corresponding to 2012 March through November. Data from Q12 are missing from
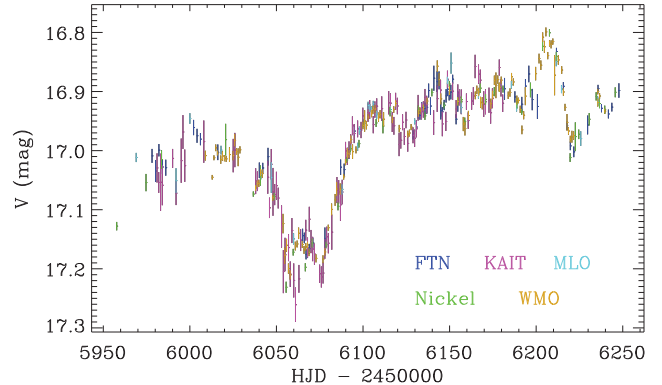


Fig. 2.— KA1858+4850 $V$-band light curve. The vertical length at each epoch indicates the photometric uncertainties.

| UT Date | Telescope | HJD $-$ 2450000 | $V$ (mag) |
|---|---|---|---|
| 2012-01-31 | N | 5957.754 | $17.129 \pm 0.008$ |
| 2012-02-11 | M | 5969.014 | $17.012 \pm 0.015$ |
| 2012-02-17 | N | 5974.663 | $17.055 \pm 0.015$ |
| 2012-02-20 | F | 5978.153 | $17.011 \pm 0.014$ |
| 2012-02-22 | F | 5980.166 | $17.037 \pm 0.020$ |

Note. — The telescopes are listed as follows: N = Nickel, M = MLO, F = FTN, K = KAIT, W = WMO. (Full table available in online version.)

the archive because, during this time, the source fell on Module 3 of the *Kepler* telescope, which failed early on in the mission.

The *Kepler* light curves are mismatched between individual quarters, so we used our $V$-band light curve as a reference to scale each quarter's light curve individually. We applied a different multiplicative scale factor and additive shift to each quarterly *Kepler* light curve to bring it into agreement with ground-based observations. The multiplicative factors account for the difference in transmission between the *Kepler* and $V$-band filters, and the additive constants account for the changes in AGN-to-host galaxy flux ratio between each quarter caused by using different quarterly extraction apertures to obtain SAP fluxes.

For each epoch in the condensed $V$-band light curve, we averaged together all *Kepler* flux measurements taken within six hours of the $V$-band measurement to compose condensed *Kepler* light curves. Then for each quarter, we fitted the contemporaneous *Kepler* and $V$-band flux measurements to the equation

$$f_V = m * f_{\text{Kepler}} + b, \qquad (2)$$

where $m$ gives the multiplicative scale factor and $b$ gives the additive shift. We fitted the data using MPFITEXY to account for measurement errors in both $V$-band and *Kepler* data. Figure 3 shows the results of applying a scale factor (top panel) and a scale factor plus a shift (middle panel) to the *Kepler* light curves.

Even with a multiplicative scale factor and an additive shift, however, there are still visible discrepancies between the two sets of data. Specifically, each *Kepler* quarterly light curve tilts downward with time compared
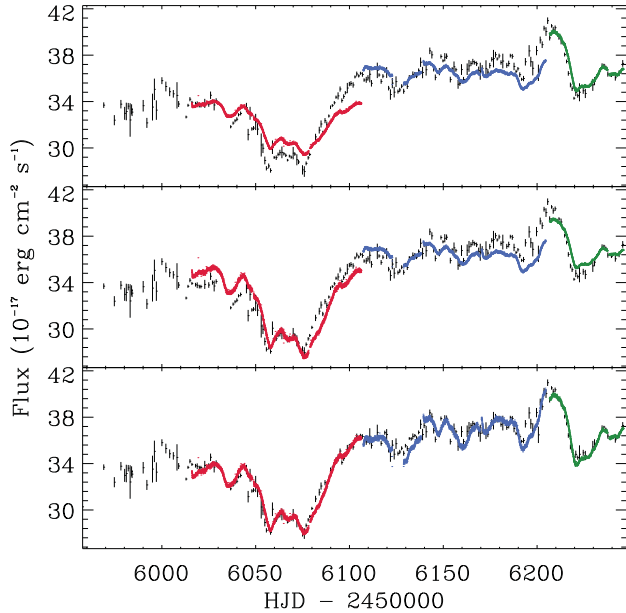
FIG. 3.— *V*-band light curve (black) overplotted with *Kepler* Q13, Q14, and Q15 light curves in red, blue, and green (respectively), scaled by three different methods. *Top:* multiplicative factor only; *middle:* multiplicative factor plus additive constant; *bottom:* multiplicative factor plus additive constant fitted to a *V*-band light curve with an additional linear trend. Error bars are not plotted for the *Kepler* points.

to the *V*-band light curve. This is caused by the constant change in *Kepler* pointing with respect to the *Kepler* field as the telescope orbited the Sun, which, in turn, causes differential velocity aberration (DVA) and results in a trend that is superimposed on the light curve within the period of each quarter (Still & Barclay 2012). To account for this effect, we applied an empirical secular linear trend to the *V*-band light curve by adding a time-dependent flux to the data. The *Kepler* light curves were then fitted to the adjusted *V*-band light curve with scale factors and shift constants. Finally, the empirical trend was removed from both *V*-band and *Kepler* light curves by subtracting the same time-dependent fluxes as before. The resulting scaled *Kepler* light curves are shown in the bottom panel of Figure 3, and were used for subsequent *Kepler*-related lag analyses.

We note that the *Kepler* passband is much better matched to the *R* band rather than the *V* band, which means there could be color-dependent variability signals contributing to discrepancies between the *V* and *Kepler* light curves. We also note that the SAP light curves from the *Kepler* archive are susceptible to several instrumental effects. First, the use of different sized apertures between individual quarters affects the SAP fluxes more so than the *Kepler* Pre-search Data Conditioning Simple Aperture Photometry (PDCSAP) fluxes because of the much smaller aperture sizes of SAP. Additionally, the effects of DVA are also larger in the SAP light curves compared to the PDCSAP light curves. A more robust analysis of *Kepler* AGN data would require re-extracting the SAP light curve over a larger set of pixels to remove these systematics, but that is beyond the scope of this work.

### 3.3. *Continuum Light Curve Characteristics*

To quantify the observed KA1858+4850 continuum variability during our monitoring period, we computed the statistics $R_{max}$ and $F_{var}$ for consistency with previous reverberation mapping studies (Rodriguez-Pascual et al. 1997; Peterson et al. 2004). $R_{max}$ is defined as the ratio between the maximum and minimum observed fluxes, and $F_{var}$ is defined as

$$F_{var} = \frac{\sqrt{\sigma^2 - \langle \delta^2 \rangle}}{\langle f \rangle}, \qquad (3)$$

where $\sigma^2$ is the sample variance, $\langle \delta^2 \rangle$ is the mean square value of the measurement uncertainties, and $\langle f \rangle$ is the unweighted mean flux. $F_{var}$ is essentially an estimate of the intrinsic root-mean-square (rms) variability relative to the mean flux corrected for random errors. We found $R_{max} = 1.56$ and $F_{var} = 0.086$ for the *V*-band light curve and $R_{max} = 1.45$ and $F_{var} = 0.080$ for the *Kepler* light curve.

A previous AGN monitoring campaign carried out by the LAMP 2008 collaboration observed 13 AGNs over a two-month period (Bentz et al. 2009). Five of these AGNs (Mrk 142, Mrk 1310, Mrk 202, NGC 4253, and NGC 4748) are NLS1 galaxies with full width at half-maximum intensity FWHM($H\beta_{broad}$) < 2000 km s$^{-1}$. The $F_{var}$ values for their *V*-band light curves range from 0.27 to 0.73, and the $R_{max}$ values range from 1.12 to 1.39. Compared to these NLS1s, KA1858+4850 was significantly more variable during our monitoring period, with both $F_{var}$ and $R_{max}$ values much larger than those for the LAMP 2008 NLS1 galaxies over their two-month monitoring period.

### 4. SPECTROSCOPIC OBSERVATIONS

Spectroscopic observations of KA1858+4850 were carried out using the Kast Spectrograph on the Shane 3-m telescope at Lick Observatory. This spectrograph is usually mounted only during dark runs. We employed an interrupt-mode observing method, where every group of Kast observers took one exposure of KA1858+4850 on each of their regularly scheduled observing nights. This enabled us to spectroscopically monitor the AGN for a total of nine months, much longer than what is achievable by most dedicated observing campaigns at classically scheduled facilities.

The Kast spectrograph has a D55 dichroic that splits light from the slit at about 5500 Å into separate blue- and red-side cameras. Our standard setup used a 600/4310 grism on the blue side, which gives a wavelength dispersion of 1.02 Å pixel$^{-1}$ and wavelength range of 2090 Å. However, the wavelength coverage was inconsistent because each group used a slightly different blue-side setup that shifted the wavelength coverage, and on the nights of 2012 February 16, 2012 March 4, 2012 April 19, and 2012 May 1, the observers employed a 830/3460 grism. We used the wavelength range 4000−5500 Å for our analysis as this is common to all spectra. This wavelength range includes the H$\beta$, H$\gamma$, H$\delta$, [O III], and He II emission lines, as well as a portion of the Balmer continuum.

On the red side, because different observing teams used significantly different setups for their primary science targets, we were unable to obtain a complete set of spectra
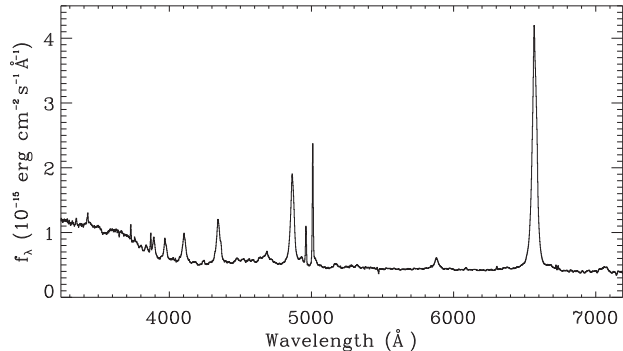
FIG. 4.— Mean rest-frame spectrum of KA1858+4850 constructed from all nights with both blue- and red-side Kast observations.



FIG. 5.— KA1858+4850 mean spectrum (black), the combined model fit of all components (red), and individual spectral fit components. The Hγ and [O III] λ4363 blend was excluded from the fits in order to limit the total number of fit parameters.

with consistent quality and wavelength coverage for analysis of the Hα line. For reference, Figure 4 shows the unweighted mean AGN spectrum constructed from all nights with both blue- and red-side Kast data.

From February to November of 2012, weather permitting, each regularly scheduled group of Kast observers took at least one 1200 s exposure of KA1858+4850 at the parallactic angle (Filippenko 1982) using a 2″ slit, along with one 120 s exposure of a flux-standard star with the same slit width for calibration. Two consecutive exposures of KA1858+4850 were taken on two nights and three consecutive exposures were taken on four nights. The flux standards we used are BD+284211, Feige 34, G191B2B, and HZ 44, in decreasing order of frequency. Very few spectra were taken in February and March owing to poor weather conditions. April and May had several good nights of data, and starting from June until the end of the campaign in November, we obtained spectra during more than two-thirds of the Kast nights each month. We obtained spectroscopic data from a total of 74 nights.

## 5. SPECTROSCOPIC REDUCTIONS AND MEASUREMENTS

Spectroscopic data reduction included overscan subtraction, flat fielding, cosmic ray cleaning using the L.A.Cosmic routine (van Dokkum 2001), extraction with a width of 6″.88 (corresponding to a 16-pixel extraction window for the blue-side data), wavelength calibration employing line-lamp exposures, and flux calibration using standard stars. We took unweighted extractions for AGN spectra and optimal extractions for standard-star spectra. Spectra taken on the same night were averaged into a single spectrum. We also propagated the extracted error spectrum through subsequent calibrations and analyses.

We attempted to perform spectral decomposition using methods described by Barth et al. (2013) to isolate the broad-line components. However, owing to the presence of weak and blended emission lines as well as limited spectral coverage, many single-epoch spectra produced poorly constrained fit parameters for the continuum components, He II and Fe II emission, and reddening. We therefore used the traditional approach of measuring line fluxes by employing a linear fit to approximately subtract the continuum underlying emission lines. The decomposed components of the higher-SNR mean spectrum are displayed in Figure 5 for reference.
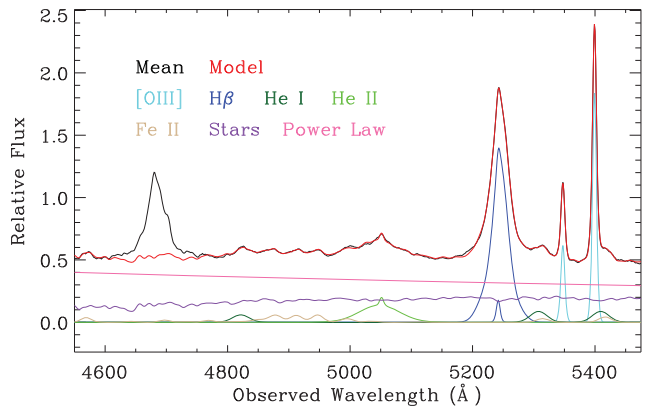
To quantify the flux-measurement uncertainty introduced by using this linear interpolation approach as opposed to the spectral deomposition method, we also measured $f(\mathrm{H}\beta)$ of a series of Hβ-only spectra. Each Hβ-only spectrum was created by subtracting from the data all model fit components except the broad and narrow Hβ models. We found that $f(\mathrm{H}\beta)$ measured from the Hβ-only spectra are, on average, 1.2% higher than those measured by simply interpolating over the continuum in the data.

To calibrate the relative fluxes between individual spectra, we followed steps described by van Groningen & Wanders (1992), where the [O III] lines are taken to be constant in flux for the duration of the campaign. As the [O III] line is emitted by gas in the narrow-line region, which is much farther out from the black hole than the BLR, the time delay in line response to continuum variations is much longer than typical reverberation mapping campaigns. The algorithm applies a multiplicative flux scaling factor, a small wavelength shift, and a convolution with a Gaussian kernel to a region in each individual spectrum that contains a narrow emission line and some surrounding continuum, and searches for a combination of these parameters that minimizes the residual between this region in the individual spectrum and the same region in a reference spectrum. We constructed the reference spectrum from the mean of all Kast blue-side spectra taken with the 600/4310 grism, and chose the observed wavelength range 5390−5410 Å, which encompasses the [O III] λ5007 emission line, to be the comparison region. Spectra taken with the 830/3460 grism were not used to make the reference spectrum, but were calibrated using the same method. The flux scale factors range from 0.27 to 4.70. The median wavelength shift is 1.2 Å, which is consistent with the amount expected from miscentering the AGN in the slit.

We followed steps described by Barth et al. (2011) to assess the accuracy of the spectral scaling, and calculated the normalized excess variance of the [O III] emission-line light curve. The normalized excess variance, $\sigma^2_{\mathrm{nx}}$, is defined by normalizing Eq. 1 by a factor of the mean flux squared, giving

TABLE 3
Wavelength Windows for Flux Measurements

| Line (Å) | Line Window (Å) | Continuum Windows (Å) |
|---|---|---|
| H$\beta$ | 5200−5290 | 5130−5160, 5360−5390 |
| He II | 4990−5100 | 4960−4980, 5120−5160 |
| H$\gamma$ | 4650−4720 | 4600−4640, 4730−4780 |
| H$\delta$ | 4395−4455 | 4360−4380, 4470−4500 |
| H$\beta$-blue | 5200−5238 | 5130−5160, 5360−5390 |
| H$\beta$-core | 5239−5249 | 5130−5160, 5360−5390 |
| H$\beta$-red | 5250−5290 | 5130−5160, 5360−5390 |

Note. — Wavelengths are in the observed frame.

$$\sigma_{\mathrm{nx}}^2 = \frac{1}{N\mu^2} \sum_{i=1}^{N} [(X_i - \mu)^2 - \sigma_i^2]. \qquad (4)$$

We found $\sigma_{\mathrm{nx}} \approx 0.02$ for the [O III] light curve after flux scaling, indicating that, above the uncertainties from photon counting in flux measurements, there is an additional scatter on the order of 2% of the total [O III] flux in the scaled light curve. This scatter may be caused by a combination of variations in seeing, miscentering of the AGN in the slit, and nightly variations in the instrument focus. Overall, this is a relatively small effect on the flux scaling of the H$\beta$ light curve. We added this 2% flux scatter in quadrature to all spectroscopic flux uncertainties before performing further analysis.

The spectroscopic data were photometrically calibrated by carrying out synthetic $V$-band photometry on the spectrum from 2012 September 9, which was taken under nearly photometric conditions. We compared this magnitude to the aperture photometry magnitude from the same night and calculated a scale factor of 1.15 that needed to be applied to the spectrum to bring the synthetic photometry measurement into agreement with the aperture photometry measurement. We then applied this scale factor to the entire set of Kast spectra.

To obtain emission-line fluxes, we first subtracted a local linear continuum surrounding the line, then integrated over the emission-line profile. Table 3 shows the wavelength ranges used for each line and their local continuum windows. Table 4 gives the spectroscopic measurements of the H$\beta$, H$\gamma$, H$\delta$, and He II emission lines for the entire dataset, as well as the SNR for each epoch measured using the observed wavelength range 4500−4600 Å. The median SNR per pixel is 28.

Figure 6 displays the $V$-band photometric and spectroscopic light curves for the H$\beta$, H$\gamma$, H$\delta$, and He II emission lines. The scaling routine works best for wavelength ranges closest to the [O III] emission lines, so at wavelengths farther away from [O III], the higher-order Balmer-line light curves become progressively noisier. Noise in the He II light curve is primarily caused by weak line strength as well as a lack of true continuum surrounding the line. The presence of Fe II lines blended into the blue side of He II, and the fact that the He II line is intrinsically very weak and broad, make fitting the true continuum with a linear model very difficult. The spectral decomposition components of He II are also poorly constrained owing to the line's low amplitude.

Figure 6 also illustrates the spectroscopic light curve for the observed wavelength range 4500−4600 Å. This region is dominated by continuum emission, so its light curve can be compared with the $V$-band light curve. This spectroscopic $B$-band continuum light curve, denoted by $B_{\mathrm{s}}$, is noisier than that of the $V$ band owing to higher susceptibility to seeing variations and slit losses, but the two light curves show consistent variability trends during the monitoring period.

The $F_{\mathrm{var}}$ and $R_{\mathrm{max}}$ values for each of the light curves are listed in Table 5. The higher-order Balmer lines exhibit distinctly larger relative variability amplitude, and the He II line is proportionally more variable than all the Balmer lines. Both results are in agreement with findings of previous reverberation mapping programs (Peterson & Ferland 1986; Dietrich et al. 1993; Kollatschny 2003; Bentz et al. 2010).

Figure 7 shows the mean and rms spectra of KA1858+4850 constructed from all blue-side spectra taken with the 600/4310 grism after applying [O III] spectral scaling. The rms spectrum indicates the amount of relative variability at each wavelength. The [O III] narrow lines have low residuals in the rms spectrum, indicating good spectral flux calibration results using the [O III] lines. The broad Balmer lines clearly stand out with very high variability. He II appears to be highly variable in the rms spectrum, even though the line is weak in the mean spectrum owing to blending with Fe II lines.

## 6. LAG MEASUREMENTS

### 6.1. Cross-Correlation Measurements

We calculated the lag between the continuum and each emission-line light curve illustrated in Figure 6, as well as between the photometric and spectroscopic light curves, by employing the interpolation cross-correlation technique developed by Gaskell & Peterson (1987) and described by White & Peterson (1994), Peterson et al. (2004), and Bentz et al. (2009). We computed the cross-correlation function (CCF) for $\tau$ values from −20 to 40 days in increments of 0.25 days. The lag for each emission line is then calculated in two ways: by using the peak of the CCF, defined as $\tau_{\mathrm{peak}}$, and by using the centroid of CCF values above 80% of the peak value, defined as $\tau_{\mathrm{cen}}$. We opted to use $\tau_{\mathrm{cen}}$ for $M_{\mathrm{BH}}$ estimates as Peterson et al. (2004) showed that this yields more consistent black hole mass estimates between different emission lines.

In cases where the continuum light curve exhibits distinct global trends, a detrending procedure is sometimes applied prior to cross-correlation analysis, where a linear function is fitted to and subtracted from the light curve so that only local variations are taken into account in the cross-correlation. We computed the H$\beta$ lag both with and without detrending using a linear fit. In the case without detrending, the lag uncertainties are smaller and the CCF peak is higher, indicating a more robust CCF. Therefore, we chose to omit the detrending procedure for our final cross-correlation analysis. The top panel in Figure 8 shows the CCF for the four emission-line light curves with the photometric light curve. We also computed the auto-correlation function (ACF) for the photometric light curve, which peaks at zero lag as expected.

To determine the final lags and their uncertainties, we employed the same Monte Carlo bootstrapping

TABLE 4
Spectroscopic Measurements for KA1858+4850

| UT Date | HJD−2450000 | SNR | $f(H\beta)$ | $f(H\gamma)$ | $f(H\delta)$ | $f(He\ II)$ |
|---|---|---|---|---|---|---|
| | | | | | $(10^{-15}\ \mathrm{erg\ cm^{-2}\ s^{-1}})$ | |
| 2012-02-16 | 5974.087 | 11 | $42.87 \pm 0.38$ | $19.12 \pm 0.51$ | $8.27 \pm 0.54$ | $11.60 \pm 0.47$ |
| 2012-03-04 | 5991.073 | 35 | $40.90 \pm 0.14$ | $18.37 \pm 0.14$ | $9.84 \pm 0.14$ | $7.30 \pm 0.14$ |
| 2012-04-02 | 6020.024 | 19 | $42.42 \pm 0.30$ | $19.30 \pm 0.27$ | $12.24 \pm 0.27$ | $9.68 \pm 0.28$ |
| 2012-04-16 | 6033.929 | 21 | $45.20 \pm 0.28$ | $22.75 \pm 0.26$ | $13.73 \pm 0.26$ | $10.20 \pm 0.27$ |
| 2012-04-16 | 6034.975 | 34 | $46.41 \pm 0.19$ | $22.53 \pm 0.16$ | $13.15 \pm 0.16$ | $8.04 \pm 0.16$ |

NOTE. — Listed SNR is the signal-to-noise ratio per pixel for the observed wavelength range 4500–4600 Å in the AGN spectra. Measured fluxes include the blended broad and narrow emission lines. (Full table available in online version.)

TABLE 5
Light Curve Statistics

| Light Curve | $F_{var}$ | $R_{max}$ |
|---|---|---|
| $V$ | 0.084 | $1.50 \pm 0.05$ |
| $B_s$ | 0.119 | $1.88 \pm 0.07$ |
| $H\beta$ | 0.076 | $1.41 \pm 0.05$ |
| $H\gamma$ | 0.078 | $1.52 \pm 0.07$ |
| $H\delta$ | 0.111 | $2.19 \pm 0.13$ |
| He II | 0.245 | $3.54 \pm 0.26$ |

NOTE. — $R_{max}$ and $F_{var}$ values for $V$, $B_s$, and the four emission lines. Higher-ionization lines show larger variations.

TABLE 6
Observed-Frame Lag Measurements

| Emission Line | $\tau_{peak}$ (days) | $\tau_{cen}$ (days) | $\tau_{\mathrm{JAVELIN}}$ (days) |
|---|---|---|---|
| $H\beta$ vs. $V$ | $8.25^{+7.25}_{-1.00}$ | $14.58^{+2.19}_{-2.50}$ | $14.18^{+1.16}_{-1.08}$ |
| $H\gamma$ vs. $V$ | $7.50^{+2.00}_{-1.25}$ | $10.96^{+3.08}_{-2.76}$ | $10.04^{+1.42}_{-1.48}$ |
| $H\delta$ vs. $V$ | $6.50^{+1.75}_{-2.00}$ | $6.42^{+2.53}_{-2.60}$ | $5.81^{+1.06}_{-2.03}$ |
| He II vs. $V$ | $0.75^{+0.50}_{-0.50}$ | $-0.58^{+1.20}_{-0.85}$ | $-2.86^{+2.01}_{-0.08}$ |
| $H\beta$ blue vs. $V$ | $7.25^{+1.00}_{-0.75}$ | $13.43^{+2.17}_{-2.62}$ | $13.85^{+1.22}_{-1.23}$ |
| $H\beta$ core vs. $V$ | $15.00^{+3.75}_{-6.50}$ | $15.50^{+1.92}_{-2.01}$ | $14.73^{+0.90}_{-0.89}$ |
| $H\beta$ red vs. $V$ | $8.50^{+5.75}_{-1.25}$ | $12.89^{+3.64}_{-3.20}$ | $14.25^{+1.28}_{-1.26}$ |
| $H\beta$ vs. $B_s$ | $11.50^{+5.50}_{-4.00}$ | $14.89^{+4.19}_{-5.10}$ | $15.67^{+1.20}_{-1.62}$ |
| $V$ vs. $B_s$ | $2.25^{+1.25}_{-2.75}$ | $1.68^{+2.21}_{-1.39}$ | $1.64^{+0.30}_{-0.73}$ |
| $H\beta$ vs. $Kepler$ | $8.25^{+6.50}_{-1.00}$ | $14.17^{+2.26}_{-2.66}$ | $13.42^{+1.10}_{-1.10}$ |
| $H\gamma$ vs. $Kepler$ | $6.75^{+1.50}_{-1.25}$ | $9.49^{+3.02}_{-2.24}$ | $9.10^{+0.93}_{-0.89}$ |
| $H\delta$ vs. $Kepler$ | $4.50^{+1.75}_{-1.75}$ | $4.86^{+2.78}_{-2.27}$ | $4.86^{+0.86}_{-0.73}$ |
| He II vs. $Kepler$ | $0.00^{+0.50}_{-0.75}$ | $-0.72^{+0.72}_{-0.72}$ | $0.88^{+0.03}_{-0.03}$ |
| $Kepler$ vs. $V$ | $0.50^{+0.25}_{-0.00}$ | $1.00^{+0.47}_{-0.47}$ | $0.76^{+0.31}_{-0.30}$ |
| $Kepler$ vs. $B_s$ | $1.75^{+1.50}_{-1.25}$ | $1.95^{+1.28}_{-1.16}$ | $2.06^{+0.15}_{-2.15}$ |

NOTE. — Cross-correlation $\tau_{peak}$, cross-correlation $\tau_{cen}$, and JAVELIN lags. Observed-frame lags can be converted to rest-frame lags by dividing by $1 + z$.

method used by Barth et al. (2011) and described by White & Peterson (1994) and Peterson et al. (2004). We constructed $10^4$ modified realizations of the continuum and emission-line light curves. Each realization is made by randomly choosing $n$ data points from the actual light curve allowing resampling, where $n$ is the total number of points in the dataset. If a point is picked $m$ times, then its uncertainty is reduced by a factor of $m^{1/2}$. The simulated light curves are then varied by adding random Gaussian noise based on the measured uncertainties at each data point. We then computed the CCF for each pair of simulated continuum and line light curves to construct distributions of $\tau_{cen}$ values. The median values are chosen as the final lag results, and the uncertainties on $\tau_{cen}$ are the $1\sigma$ thresholds in the distribution centered around the median.

Table 6 gives the measured $\tau_{peak}$ and $\tau_{cen}$ values for the four emission-line light curves with respect to the $V$-band light curve. The He II lag is consistent with zero within $1\sigma$ uncertainties. The larger fractional uncertainties on the higher-order Balmer line lags, as well as on the He II lag, can be attributed to their noisier light curves due to less precise spectral scaling at wavelengths farther from [O III].

The lag times are progressively shorter for higher-order Balmer lines. Specifically, we find lag ratios of $\tau(H\beta):\tau(H\gamma):\tau(H\delta)=1.00:0.75:0.44$. This is consistent with the picture of a BLR stratified in optical depth (Rees et al. 1989; Korista & Goad 2004), as well as with findings from previous reverberation mapping campaigns (e.g., Bentz et al. 2010).

Additionally, we attempted to obtain velocity-resolved lag measurements for KA1858+4850, since the lag behavior as a function of velocity across broad emission lines can contain information about BLR kinematics. We divided the $H\beta$ line profile into three wavelength segments: $5200-5238$ Å for the blue wing, $5239-5249$ Å for the core, and $5250-5290$ Å for the red wing. The $H\beta$ lag for

each segment is listed in Table 6. We found marginal evidence for longer lag in the emission-line core and shorter lags in the wings. We were unable to obtain useful lag measurements for smaller velocity bins, and therefore refrain from drawing any definitive conclusions regarding the kinematics of the BLR.

### 6.2. *JAVELIN*

We used an alternative method of estimating emission-line lags, which employs a statistical model for quasar variability. This method uses the *Python* code JAVELIN v.0.3$\alpha$ (Zu et al. 2011) to model the optical AGN continuum variability as a damped random walk process with covariance function

$$S_{\mathrm{DRW}}(\Delta t) = \sigma^2 \exp\left(-\left|\frac{\Delta t}{\tau_r}\right|\right), \qquad (5)$$

where $\tau_r$ is the "relaxation time" required for the variability to become roughly uncorrelated, and $\sigma$ is the variability amplitude on timescales much shorter than $\tau_r$ (Kelly et al. 2009). JAVELIN fits $\tau_r$ and $\sigma$ for the AGN continuum light curve, then models the emission-line light curves as lagged, smoothed, and scaled versions of the continuum light curve. An important caveat of using JAVELIN for the KA1858+4850 lag analysis is that the Kelly et al. (2009) damped random walk model pro-
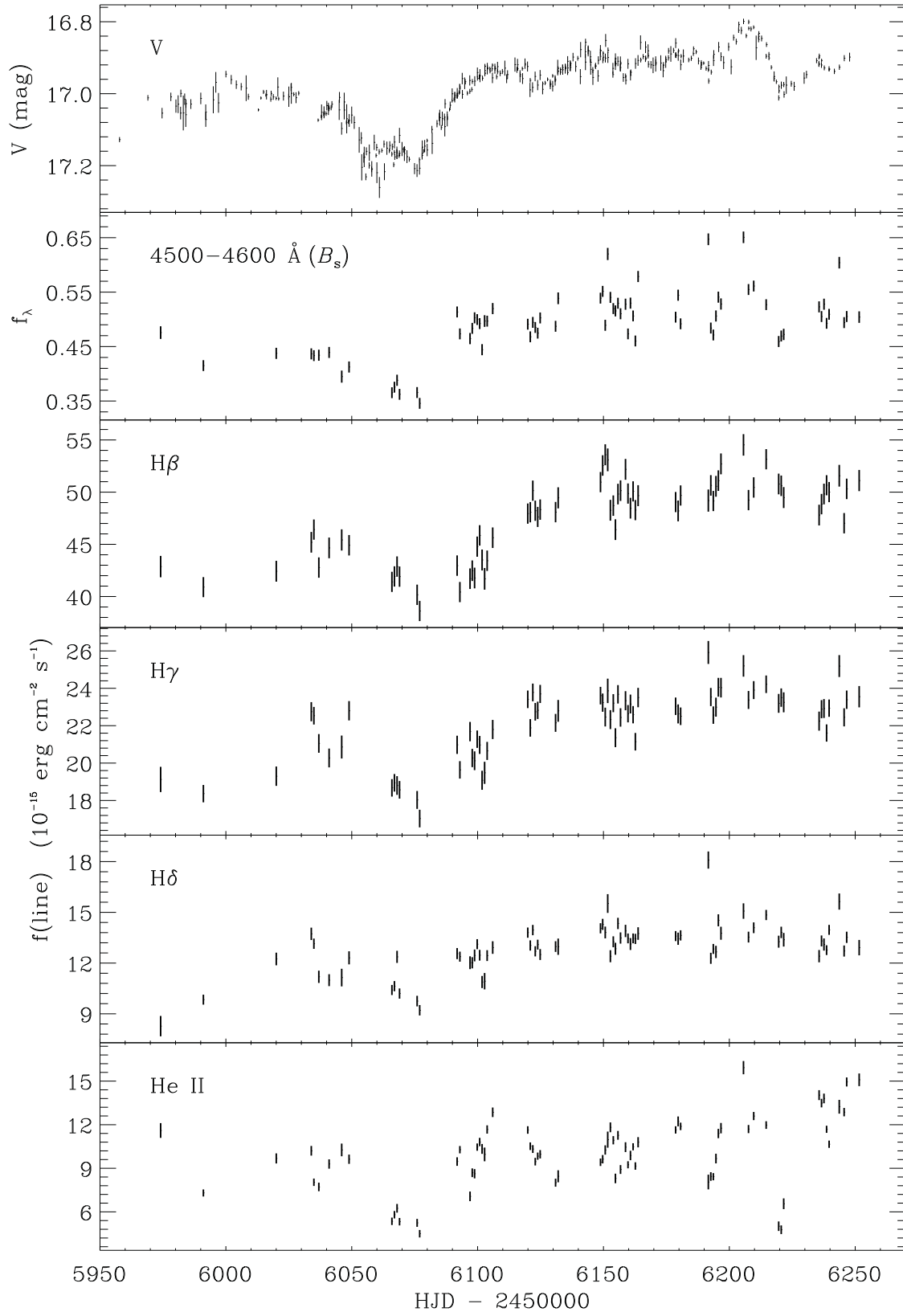
Fig. 6.— KA1858+4850 $V$-band magnitude, continuum flux measured from the spectroscopic data, and emission-line light curves. Plotted errors include the 2% flux scatter found by computing the normalized excess variance of the [O III] light curve.
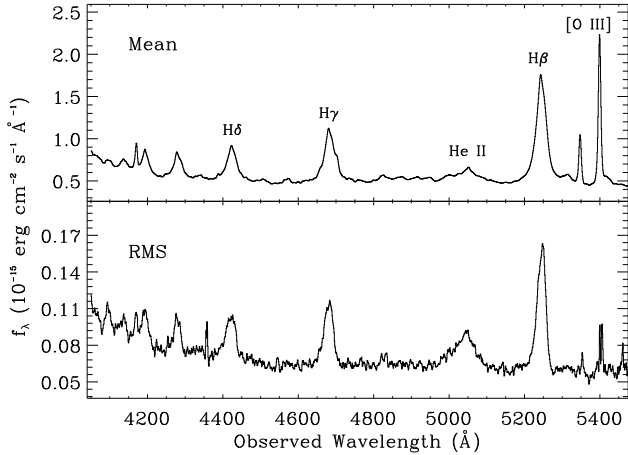
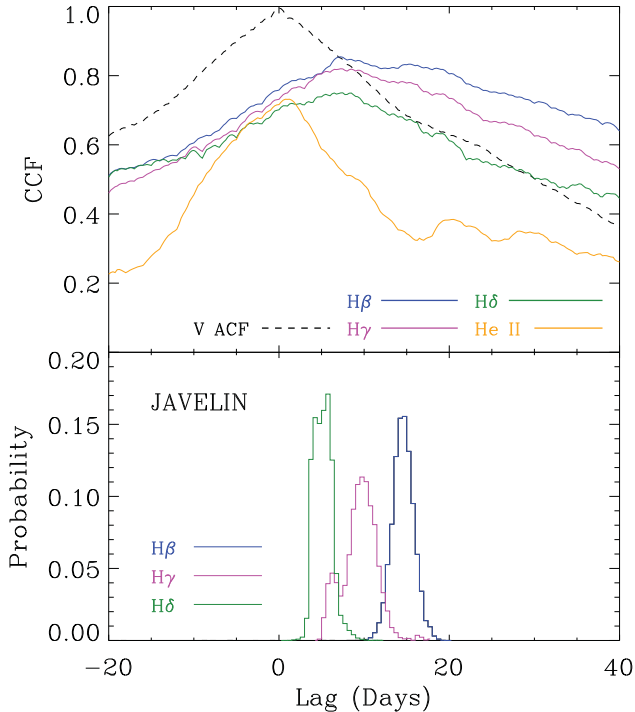FIG. 7.— Mean and rms spectra of KA1858+4850.



FIG. 8.— *Top*: Cross-correlation functions between the four emission lines and the *V*-band continuum, and the auto-correlation function of the *V*-band continuum. *Bottom*: Probability distributions of JAVELIN lags for Hβ, Hγ, and Hδ. These distributions were obtained with $6.25 \times 10^4$ iterations, while the He II distribution was obtained with $2.5 \times 10^5$ iterations. However, the He II distribution is poorly constrained owing to the line's noisy light curve, and is therefore omitted in this plot.

duces variability power spectra with a slope of $-2$, while Mushotzky et al. (2011) showed that KA1858+4850 has a power-spectrum slope of $\sim -3$.

The *V*-band light curve was rebinned into one-day intervals for analysis with JAVELIN in order to cut down on computation time. While JAVELIN is, in principle, able to fit a large number of emission-line light curves simultaneously, the lags were poorly constrained in this case for fitting three emission-line light curves simultaneously, most likely because of the monthly gaps in the data when the Moon was bright. Therefore, we chose the
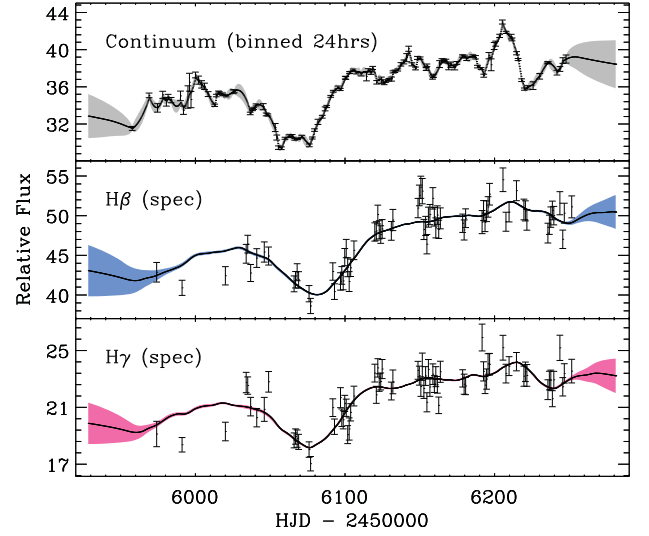


FIG. 9.— JAVELIN model results for the continuum (*V* band), Hβ (spectroscopic), and Hγ (spectroscopic) light curves (black solid lines), the model $1\sigma$ uncertainties at each time (shaded regions), and observational data and uncertainties.

two-line analysis method, where we fit each of Hγ, Hδ, and He II emission-line light curves simultaneously with that of Hβ. The Hβ lags computed from pairing with Hγ and Hδ are consistent with each other, while the Hβ lag computed from pairing with He II yielded a slightly shorter lag. This is likely due to the noisy He II light curve as well as the fact that He II intrinsically has a lag that is very short compared to the monthly gaps in the light curves, which makes the lag difficult to measure. We use the Hβ lag value obtained from pairing with Hγ as $\tau_{\text{JAVELIN}}$ for Hβ.

Table 6 lists the JAVELIN lags, which are consistent with those obtained using cross-correlation techniques within $1\sigma$ uncertainties. Lags for the Hβ blue wing, core, and red wing were computed simultaneously in a three-line JAVELIN run, and the *V*-band and Hβ lags with respect to the $B_s$ band were obtained from a two-line run. The bottom panel of Figure 8 shows the JAVELIN distributions for Hβ, Hγ, and Hδ lags, and Figure 9 shows the JAVELIN model results for the continuum, Hβ, and Hγ light curves.

We note that both the CCF and JAVELIN He II lags are slightly negative, which is likely caused by the combined effects of the higher ionization (and therefore shorter lag) of He II, and a slight contaminating lag signal in the *V*-band light curve, described in the next section.

### 6.3. Hβ Contamination in the V band

There is a small biasing factor in the Hβ lag calculations from the emission-line contribution to the *V*-band flux. While the *V*-band light curve would ideally represent pure continuum, the presence of the Hβ line in the *V* filter adds a flux component that contains a lag signal. Consequently, the calculated lags from the biased continuum would be shorter than those obtained with a pure continuum.

To determine the magnitude of this contribution, we first combined the blue- and red-side spectra from a single night, and next performed synthetic photometry on the spectrum using a Johnson *V* filter. We then removed

the H$\beta$ line from the spectrum by directly interpolating over it, performed synthetic photometry on the modified spectrum, and compared the two magnitude results. We found that H$\beta$ contributes approximately 9.6% of the $V$-band flux, and assume that H$\beta$ dominates the variable emission-line contribution in the $V$ band and is therefore the main source of the lag bias.

To quantify the effect of this bias on the calculated lag, we simulated $10^4$ pure AGN continuum light curves using methods described by Timmer & Koenig (1995), and simulated corresponding emission-line light curves by convolving the continuum light curves with a $\delta$ function at a lag of 14 days. We then simulated $10^4$ contaminated $V$-band light curves by adding a lagged emission-line contribution to the continuum at the 9.6% level. The pure and contaminated continuum light curves in each pair are both then cross-correlated with the corresponding emission-line light curve to create two distributions of lag times. We found a median lag of $14.0 \pm 2.1$ days for the pure continuum case and a median lag of $13.2 \pm 2.1$ days for the contaminated continuum case, indicating an expected bias of 0.8 days. This prediction is similar to the bias we find from observations.

We found an H$\beta$ lag of $14.89^{+4.19}_{-5.10}$ days with respect to $B_{\rm s}$, which contains no H$\beta$ flux contamination, indicating an observed bias of $\sim$0.3 days compared to the lag-contaminated case. We also found a small positive lag of $1.68^{+2.21}_{-1.39}$ days for the $V$ light curve with respect to $B_{\rm s}$. However, in both simulations and observations, the biases are smaller than the lag uncertainties for H$\beta$ with respect to the $V$-band light curve. We therefore conclude that the lag bias due to H$\beta$ flux contribution in the $V$ band is present, but is small compared to the $1\sigma$ uncertainties on the $\tau_{\rm cen}$ measurements.

### 6.4. Lags with Respect to Kepler Light Curve

We computed the lag of each emission line with respect to the scaled *Kepler* fluxes using both cross-correlation analysis and JAVELIN. The *Kepler* light curve has a cadence of 30 minutes, giving a total of $\sim 1.3 \times 10^4$ data points over three quarters. We binned the light curve into bins of 12 and 24 hours to use in the cross-correlation and JAVELIN analyses, respectively. For both CCF and JAVELIN, we found the emission-line lags with respect to the *Kepler* light curve, listed in Table 6, to be consistent with but slightly shorter than those with respect to the $V$-band continuum. This is consistent with expectations, since the *Kepler* passband includes H$\alpha$, which introduces an additional lag signal to the *Kepler* light curve compared to the $V$-band data. The redder portion of the continuum could also have a small lag with respect to the bluer continuum (Sergeev et al. 2005), since the redder continuum emission comes from larger radii in the accretion disk than where the $V$-band continuum is emitted. The combined effects of broad emission lines and red continuum in the *Kepler* band should account for the shorter emission-line lags measured against the *Kepler* light curve as compared to those measured against the $V$-band light curve.

We also measured the lag of the *Kepler* light curve with respect to both the $V$-band and $B_{\rm s}$-band light curves, and found small positive lags for both cases. This also supports the idea of broad emission lines and the red continuum introducing a lag signal to the *Kepler* light

curve.

## 7. LINE WIDTHS AND BLACK HOLE MASS ESTIMATE

There are two conventional methods of measuring the broad-line width: using the FWHM and the line dispersion ($\sigma_{\rm line}$) of the emission-line profile. The line profile is typically taken to be the rms profile, since using the variable portion of the spectrum instead of the mean spectrum implies a black hole mass estimate based only on components of the emission line that echo the continuum signal (Peterson et al. 2004). The line dispersion is defined as

$$\sigma_{\rm line}^2 = \left(\frac{c}{\lambda_0}\right)^2 \left(\frac{\sum \lambda_i^2 S_i}{\sum S_i} - \lambda_0^2\right), \qquad (6)$$

where $S_i$ is the flux density at wavelength bin $\lambda_i$ and $\lambda_0$ is the flux-weighted centroid wavelength of the line profile. In this empirical method of measuring the line width, the line profile is not fitted to any functional model. We used the same line and continuum windows to measure the line width as those used in measuring line fluxes.

To determine the final FWHM and $\sigma_{\rm line}$ values and uncertainties, we employed the bootstrap method described by Peterson et al. (2004). The entire dataset contains $N$ spectra. For each bootstrap realization, we randomly selected $N$ spectra from the dataset allowing reselection, constructed the mean and rms line profiles from this randomly sampled set, and measured the line dispersion of the rms profile. From multiple realizations, we built up a distribution of FWHM and line-dispersion values, and took the median and standard deviation of the distributions to be the final FWHM and $\sigma_{\rm line}$ and their uncertainties, respectively. We removed the instrumental line width by taking the width of the $\lambda$5086 Cd I calibration line in a $2''$-slit width exposure and subtracting it from the measured FWHM or $\sigma_{\rm line}$ in quadrature. We found FWHM = 324 km s$^{-1}$ for the Cd I calibration line for a Gaussian fit to the line profile. After correcting for the instrumental line width, we found FWHM = $1511 \pm 68$ km s$^{-1}$ and $\sigma_{\rm line} = 770 \pm 49$ km s$^{-1}$ for the H$\beta$ line in the rms spectrum.

We also measured the H$\beta$ FWHM and $\sigma_{\rm line}$ for the mean profile. To ensure exclusion of the narrow-line component in the width measurements, we measured the FWHM and $\sigma_{\rm line}$ of the broad H$\beta$ model based on the spectral decomposition of the mean spectrum, as shown in Figure 5. The [O III] narrow-line profile was used to model the narrow H$\beta$ line in the spectral fitting routines, and $f({\rm H}\beta_{\rm narrow})/f([{\rm O~III}]_{\lambda5007}) \approx 0.09$. We also measured the FWHM and $\sigma_{\rm line}$ of the broad H$\beta$ model for each epoch in our dataset, and took the standard deviations about the means to be the FWHM and $\sigma_{\rm line}$ uncertainties. We found FWHM = $1820 \pm 79$ km s$^{-1}$ and $\sigma_{\rm line} = 853 \pm 34$ km s$^{-1}$ for H$\beta$ in the mean spectrum after subtracting the instrumental line width. This is consistent with previous findings that line widths measured from mean spectra tend to be larger than those measured from rms spectra (e.g., Bentz et al. 2009).

The reverberation lag and line width of H$\beta$ combined can give a virial estimate of the central black hole mass, given by

$$M_{\mathrm{BH}} = f\frac{(c\tau)(\Delta V)^2}{G}, \qquad (7)$$

where $\tau$ is the H$\beta$ lag time with respect to the continuum and $c\tau$ gives the mean radius of the BLR, $\Delta V$ is the H$\beta$ line width, $G$ is the gravitational constant, and $f$ is a scaling factor of order unity that depends on the inclination and kinematics of the BLR. Traditionally, since these properties of the BLR are usually unknown, the scale factor $f$ is chosen to be a value that brings the set of reverberation mapped AGNs into agreement with local quiescent galaxies in the $M_{\mathrm{BH}} - \sigma_\star$ relation, which relates black hole mass to host-galaxy bulge stellar velocity dispersion (Onken et al. 2004; Woo et al. 2010; Park et al. 2012; Grier et al. 2013).

We use $c\tau_{\mathrm{cen}}$ for the BLR radius and H$\beta$ line dispersion $\sigma_{\mathrm{line}}$ of the rms line profile for $\Delta V$, for consistency with Peterson et al. (2004), and a scale factor of $f = 5.13$, calculated by Park et al. (2012) based on the updated local AGN $M_{\mathrm{BH}} - \sigma_\star$ relation obtained with the forward regression method. Combining the H$\beta$ vs. $V$ lag of $14.58^{+2.19}_{-2.50}$ days, corresponding to a rest-frame lag of $\tau_{\mathrm{cen}} = 13.53^{+2.03}_{-2.32}$ days, and $\sigma_{\mathrm{line}} = 770 \pm 49$ km s$^{-1}$, we obtain a virial black hole mass estimate of $M_{\mathrm{BH}} = 8.06^{+1.59}_{-1.72} \times 10^6 \ M_\odot$. If we follow the prescription of Grier et al. (2013) by using the H$\beta$ $\tau_{\mathtt{JAVELIN}}$ and a scale factor $f = 4.31$, we find $M_{\mathrm{BH,JAVELIN}} = 6.58^{+1.00}_{-0.98} \times 10^6 \ M_\odot$.

The above uncertainties on $M_{\mathrm{BH}}$ include only errors propagated from the lag and emission-line-width measurements. If we incorporate the uncertainties on the mean scale factor from the linear fits by Park et al. (2012), $f = 5.13 \pm 1.30$, then our black hole mass estimate becomes $M_{\mathrm{BH}} = 8.06^{+2.58}_{-2.67} \times 10^6 \ M_\odot$. It is evident that true uncertainties on the virial estimate of $M_{\mathrm{BH}}$ are dominated by the systematic uncertainties in the scale factor, which are significantly larger than those derived from the lag and line-width measurements alone.

We note that there are other estimates of the scale factor, such as those obtained by separating galaxies into different populations based on mass (Greene et al. 2010) and morphology (Graham et al. 2011), which yield estimates of $f$ different from that of Park et al. (2012) by up to a factor of $\sim 2$. For example, Woo et al. (2013) investigated the scale factor for both quiescent and active galaxies as a combined sample and found $f = 5.9^{+2.1}_{-1.5}$. Furthermore, recent work by Ho & Kim (2014) showed that the scale factor can be different for galaxies with pseudobulges and classical buldges, with $f = 3.2 \pm 0.7$ for pseudobulges and $f = 6.3 \pm 1.5$ for classical bulges. Various ongoing efforts that further examine the $M_{\mathrm{BH}} - \sigma_\star$ relation for local galaxies will improve the precision of the scale factor in the near future as the number of reverberation mapped AGNs increases. Moreover, there has been progress in constraining $f$ for individual galaxies by dynamically modeling the BLR (Pancoast et al. 2013).

In addition, we obtained $M_{\mathrm{BH}}$ estimates using the broad H$\gamma$ and H$\delta$ lines. No lag estimate was attempted using He II since the line has a negative lag. The line widths, rest-frame lags, and derived $M_{\mathrm{BH}}$ values are listed in Table 7. The H$\gamma$ and H$\delta$ light curves are signif-

icantly noisier than that of H$\beta$; thus, it is not surprising that, for both CCF and $\mathtt{JAVELIN}$ cases, the derived $M_{\mathrm{BH}}$ values have much higher fractional uncertainties compared to the H$\beta$ $M_{\mathrm{BH}}$. For both CCF and $\mathtt{JAVELIN}$ lags, the H$\gamma$ $M_{\mathrm{BH}}$ estimates, though consistent with the H$\beta$ $M_{\mathrm{BH}}$ values within $1\sigma$ uncertainties, are slightly smaller than those of H$\beta$, and $M_{\mathrm{BH}}$ estimates for H$\delta$ are smaller still. This may be due to the fact that we are using the same $f$ factor for all the emission lines, while the stratified nature of the BLR may imply different scale factors for each line that depend on the geometry and kinematics of the line-emitting gas.

We would like to compare KA1858+4850 to other AGNs having similar black hole masses by studying its location on the $M_{\mathrm{BH}} - \sigma_\star$ relation as well as the $M_{\mathrm{BH}} - L_{\mathrm{bulge}}$ relation (black hole mass vs. host-galaxy bulge luminosity). However, because KA1858+4850 appears point-like at ground-based resolution, it is impossible to observe structural properties of the host galaxy without high-resolution images from the *Hubble Space Telescope (HST)* or ground-based observations using adaptive optics. Additionally, our Lick spectra cannot be used to measure stellar velocity dispersion in KA1858+4850 owing to the galaxy's weak starlight component compared to its AGN luminosity.

## 8. EDDINGTON RATIO

AGNs have been observed to follow a tight correlation between the size of the BLR ($R_{\mathrm{BLR}}$) and continuum luminosity ($L_\lambda$). The $R_{\mathrm{BLR}} - L_\lambda$ relation can be written in the form

$$\log\left(\frac{R_{\mathrm{BLR}}}{1 \ \mathrm{lt\text{-}day}}\right) = K + \alpha \log\left(\frac{\lambda L_\lambda}{10^{44} \ \mathrm{erg \ s^{-1}}}\right), \qquad (8)$$

where $L_\lambda$ is measured at $\lambda_{\mathrm{rest}} = 5100$ Å. Bentz et al. (2013) found the values of $K$ and $\alpha$ to be $1.560^{+0.024}_{-0.024}$ and $0.546^{+0.027}_{-0.027}$ respectively, with a scatter of around 0.13 dex for their best fit. From these parameters and the lag for KA1858+4850, we expect to find $\lambda L_\lambda(5100 \ \text{Å}) = 1.64^{+0.59}_{-0.65} \times 10^{43}$ erg s$^{-1}$. We used combined Kast blue- and red-side spectra to measure $L_\lambda$ and adopted the spectral fitting components for the mean spectrum (shown in Figure 5) to estimate the starlight contribution in this region, which we found to be approximately 40% of the total flux. Correcting for Galactic extinction, we roughly estimate $\lambda f_\lambda(5100 \ \text{Å}) \approx 1.6 \times 10^{-12}$ erg cm$^{-2}$ s$^{-1}$ for the AGN, corresponding to $\lambda L_\lambda(5100 \ \text{Å}) \approx 2.4 \times 10^{43}$ erg s$^{-1}$ for a luminosity distance of 354 Mpc. (We assume the same standard $\Lambda$CDM cosmology as Bentz et al. 2013, where $H_0 = 72$ km s$^{-1}$ Mpc$^{-1}$, $\Omega_{\mathrm{M}} = 0.3$, and $\Omega_\Lambda = 0.7$.) This is consistent with expectations given the scatter in the fit values from Bentz et al. (2013).

KA1858+4850 is a NLS1, a class of objects thought to have high $L/L_{\mathrm{Edd}}$ (Pogge 2011, and references therein). We apply the bolometric correction used by Kaspi et al. (2000), where $L_{\mathrm{bol}} \approx 9 \lambda L_\lambda(5100 \ \text{Å})$, and obtain an estimate of $L_{\mathrm{bol}} = 2.2 \times 10^{44}$ erg s$^{-1}$ and $L/L_{\mathrm{Edd}} \approx 0.2$ using $M_{\mathrm{BH}} = 8.06^{+1.59}_{-1.72} \times 10^6 \ M_\odot$. We compared this Eddington ratio to those of the four LAMP 2008 NLS1 galaxies, which were calculated using black hole masses published by Bentz et al. (2009) and $\lambda L_\lambda(5100 \ \text{Å})$ values

TABLE 7
Line Widths, Lags, and Derived Black Hole Masses

| Emission Line | $\sigma_{\rm line}$ (km s$^{-1}$) | Lag Computation Method | $\tau_{\rm cen,rest}$ (days) | $M_{\rm BH}$ ($10^6$ $M_\odot$) |
|---|---|---|---|---|
| H$\beta$ | $770 \pm 49$ | CCF | $13.53^{+2.03}_{-2.32}$ | $8.06^{+1.59}_{-1.72}$ |
| | | JAVELIN | $13.15^{+1.08}_{-1.00}$ | $6.85^{+1.00}_{-0.98}$ |
| H$\gamma$ | $741 \pm 73$ | CCF | $10.17^{+2.86}_{-2.56}$ | $5.59^{+1.92}_{-1.79}$ |
| | | JAVELIN | $9.31^{+1.32}_{-1.37}$ | $3.99^{+0.97}_{-0.98}$ |
| H$\delta$ | $827 \pm 83$ | CCF | $5.96^{+2.35}_{-2.41}$ | $4.20^{+1.85}_{-1.89}$ |
| | | JAVELIN | $5.39^{+0.98}_{-1.88}$ | $3.19^{+0.86}_{-1.28}$ |

Note. — Line lags are measured against the $V$-band continuum. $M_{\rm BH}$ from CCF lags were calculated using $f = 5.13$ (Park et al. 2012), and $M_{\rm BH}$ from JAVELIN lags were calculated using $f = 4.31$ (Grier et al. 2013).

given in Bentz et al. (2013). After applying the same bolometric correction as for KA1858+4850, we found $L/L_{\rm Edd} = [0.5, 0.7, 1.2, 0.9]$ for Mrk 1310, Mrk 202, NGC 4253, and NGC 4748, respectively. Compared to these NLS1s, KA1858+4850 has a significantly lower Eddington ratio.

A recent study by Du et al. (2014) measured the H$\beta$ lag and $M_{\rm BH}$ of three NLS1 galaxies (Mrk 335, Mrk 142, and IRAS F12397), all of which appear spectroscopically similar to KA1858+4850. The authors compute the Eddington rate based on a thin accretion disk model (Shakura & Sunyaev 1973). This rate, denoted by $\dot{m}_{\rm ss}$, is written as

$$\dot{m}_{\rm ss} \approx 20.1 \left( \frac{L_{44}}{\cos i} \right)^{3/2} M_7^{-2} \eta_{\rm ss}, \qquad (9)$$

where they define $L_{44} = \lambda L_\lambda / 10^{44}$ erg s$^{-1}$ at $\lambda = 5100$ Å, $M_7 = M_{\rm BH}/10^7 M_\odot$, and $\cos i = 0.75$ as the inclination typical of Type 1 AGNs. For a minimal radiative efficiency of $\eta_{\rm ss} = 0.038$, they find Eddington ratios of 0.6, 2.3, and 4.6 for Mrk 335, Mrk 142, and IRAS F12397, respectively. Applying this same prescription to KA1858+4850, with $M_7 = 0.81$ and $L_{44} = 0.24$, we find $\dot{m}_{\rm ss} = 0.2$, in agreement with our $L/L_{\rm Edd}$ value obtained using the Kaspi et al. (2000) bolometric correction.

## 9. SUMMARY

We photometrically and spectroscopically monitored the $Kepler$-field AGN KA1858+4850 over a period of nine months. We found an H$\beta$ rest-frame lag of $13.53^{+2.03}_{-2.32}$ days with respect to continuum variations using cross-correlation methods, and a lag of $13.15^{+1.08}_{-1.00}$ days using the JAVELIN method. We also measured emission-line lags with respect to the $Kepler$ light curve and found slightly shorter lags compared to those measured against the $V$-band light curve, which is expected given the contributions of broad emission lines and red continuum flux to the $Kepler$ band. We measured an H$\beta$ velocity dispersion of $\sigma_{\rm line} = 770 \pm 49$ km s$^{-1}$, and calculated a black hole virial mass of $M_{\rm BH} = 8.06^{+1.59}_{-1.72} \times 10^6$ $M_\odot$ using $\tau_{\rm CCF}$ and scale factor empirically derived from local active galaxies by Park et al. (2012), and a black hole mass of $M_{\rm BH,JAVELIN} = 6.58^{+1.00}_{-0.98} \times 10^6$ $M_\odot$ using $\tau_{\rm JAVELIN}$ and scale factor taken from Grier et al. (2013). For this mass, the Eddington ratio is $L/L_{\rm Edd} \approx 0.2$.

KA1858+4850 was the second AGN for which data was obtained in this interrupt observing mode from Lick Observatory, and the second AGN in the $Kepler$ field to be monitored by ground-based telescopes (the first being Zw 229-015, Barth et al. 2011). Comparing our lag results with those obtained by the LAMP 2008 collaboration (Bentz et al. 2009), our lag uncertainties are slightly larger. However, considering the much longer lag of KA1858+4850, our H$\beta$ fractional lag precision, at less than 20%, is still very good. Our analysis using $Kepler$ light curves also offers one of the first direct comparison of reverberation mapping results between ground- and space-based observations for a $Kepler$ AGN. The success of our campaign demonstrates the robust capabilities of interrupt-mode observations for monitoring AGN variability. Factors that negatively impact our measurements, such as inconsistency in data quality and gaps in the spectroscopic light curves (in this case due to the AGN being observed only during dark runs), are mitigated by a well-sampled $V$-band light curve obtained by combining observations from several ground-based telescopes as well as the long duration of the program.

Further observations of KA1858+4850 can provide additional insight into various properties of the AGN and host galaxy. Specifically, observations of the bulge properties can put KA1858+4850 on the $M_{\rm BH} - L_{\rm bulge}$, $M_{\rm BH} - M_{\rm bulge}$, and $M_{\rm BH} - \sigma_*$ relations. Since the host galaxy is very compact, high-resolution HST or adaptive optics imaging will be needed to examine the host-galaxy morphology.

## REFERENCES

Barth, A. J., Nguyen, M. L., Malkan, M. A., et al. 2011, ApJ, 732, 121

Barth, A. J., Pancoast, A., Bennert, V. N., et al. 2013, ApJ, 769, 128

Bauer, A., Baltay, C., Coppi, P., et al. 2009, ApJ, 696, 1241

Bentz, M. C., Walsh, J. L., Barth, A. J., et al. 2009, ApJ, 705, 199

—. 2010, ApJ, 716, 993

Bentz, M. C., Denney, K. D., Grier, C. J., et al. 2013, ApJ, 767, 149

Blandford, R. D., & McKee, C. F. 1982, ApJ, 255, 419

Borucki, W. J., Koch, D., Basri, G., et al. 2010, Science, 327, 977

Brown, T. M., Baliber, N., Bianco, F. B., et al. 2013, PASP, 125, 1031

Cid Fernandes, Jr., R., Aretxaga, I., & Terlevich, R. 1996, MNRAS, 282, 1191

Collier, S., & Peterson, B. M. 2001, ApJ, 555, 775

Cristiani, S., Vio, R., & Andreani, P. 1990, AJ, 100, 56

Dietrich, M., Kollatschny, W., Peterson, B. M., et al. 1993, ApJ, 408, 416

Du, P., Hu, C., Lu, K.-X., et al. 2014, ApJ, 782, 45

Edelson, R., & Malkan, M. 2012, ApJ, 751, 52

Filippenko, A. V. 1982, PASP, 94, 715

Filippenko, A. V., Li, W. D., Treffers, R. R., & Modjaz, M. 2001, in Astronomical Society of the Pacific Conference Series, Vol. 246, IAU Colloq. 183: Small Telescope Astronomy on Global Scales, ed. B. Paczynski, W.-P. Chen, & C. Lemme, 121

Gaskell, C. M., & Peterson, B. M. 1987, ApJS, 65, 1

Giallongo, E., Trevese, D., & Vagnetti, F. 1991, ApJ, 377, 345

Giveon, U., Maoz, D., Kaspi, S., Netzer, H., & Smith, P. S. 1999, MNRAS, 306, 637

Graham, A. W., Onken, C. A., Athanassoula, E., & Combes, F. 2011, MNRAS, 412, 2211

Greene, J. E., Peng, C. Y., Kim, M., et al. 2010, ApJ, 721, 26

Grier, C. J., Martini, P., Watson, L. C., et al. 2013, ApJ, 773, 90

Ho, L. C., & Kim, M. 2014, ApJ, 789, 17

Hook, I. M., McMahon, R. G., Boyle, B. J., & Irwin, M. J. 1994, MNRAS, 268, 305

Kaspi, S., Smith, P. S., Netzer, H., et al. 2000, ApJ, 533, 631

Kelly, B. C., Bechtold, J., & Siemiginowska, A. 2009, ApJ, 698, 895

Kollatschny, W. 2003, A&A, 407, 461

Korista, K. T., & Goad, M. R. 2004, ApJ, 606, 749

Landolt, A. U. 1992, AJ, 104, 340

Lang, D., Hogg, D. W., Mierle, K., Blanton, M., & Roweis, S. 2010, AJ, 139, 1782

MacLeod, C. L., Ivezić, Ž., Kochanek, C. S., et al. 2010, ApJ, 721, 1014

Mushotzky, R. F., Edelson, R., Baumgartner, W., & Gandhi, P. 2011, ApJ, 743, L12

Onken, C. A., Ferrarese, L., Merritt, D., et al. 2004, ApJ, 615, 645

Pancoast, A., Brewer, B. J., Treu, T., et al. 2013, ArXiv e-prints, arXiv:1311.6475

Park, D., Kelly, B. C., Woo, J.-H., & Treu, T. 2012, ApJS, 203, 6

Peterson, B. M., & Ferland, G. J. 1986, Nature, 324, 345

Peterson, B. M., Ferrarese, L., Gilbert, K. M., et al. 2004, ApJ, 613, 682

Pogge, R. W. 2011, in Narrow-Line Seyfert 1 Galaxies and their Place in the Universe

Rees, M. J., Netzer, H., & Ferland, G. J. 1989, ApJ, 347, 640

Revalski, M., Nowak, D., Wiita, P. J., Wehrle, A. E., & Unwin, S. C. 2014, ApJ, 785, 60

Rodriguez-Pascual, P. M., Alloin, D., Clavel, J., et al. 1997, ApJS, 110, 9

Schlafly, E. F., & Finkbeiner, D. P. 2011, ApJ, 737, 103

Sergeev, S. G., Doroshenko, V. T., Golubinskiy, Y. V., Merkulova, N. I., & Sergeeva, E. A. 2005, ApJ, 622, 129

Shakura, N. I., & Sunyaev, R. A. 1973, A&A, 24, 337

Still, M., & Barclay, T. 2012, PyKE: Reduction and analysis of Kepler Simple Aperture Photometry data, astrophysics Source Code Library, ascl:1208.004

Timmer, J., & Koenig, M. 1995, A&A, 300, 707

van Dokkum, P. G. 2001, PASP, 113, 1420

van Groningen, E., & Wanders, I. 1992, PASP, 104, 700

Vanden Berk, D. E., Wilhite, B. C., Kron, R. G., et al. 2004, ApJ, 601, 692

Voges, W., Aschenbach, B., Boller, T., et al. 1999, VizieR Online Data Catalog, 9010, 0

Webb, W., & Malkan, M. 2000, ApJ, 540, 652

White, R. J., & Peterson, B. M. 1994, PASP, 106, 879

Wilhite, B. C., Brunner, R. J., Grier, C. J., Schneider, D. P., & vanden Berk, D. E. 2008, MNRAS, 383, 1232

Wold, M., Brotherton, M. S., & Shang, Z. 2007, MNRAS, 375, 989

Woo, J.-H., Schulze, A., Park, D., et al. 2013, ApJ, 772, 49

Woo, J.-H., Treu, T., Barth, A. J., et al. 2010, ApJ, 716, 269

Zu, Y., Kochanek, C. S., & Peterson, B. M. 2011, ApJ, 735, 80